Rare Metal Materials and Engineering
Volume 48, Issue 3, March 2019
Available online at www.rmme.ac.cn

Science Press

Cite this article as: Rare Metal Materials and Engineering, 2019, 48(3): 0788-0796.

ARTICLE

Low-cycle Fatigue Properties of Friction Stir Welding Joint of AZ31 Magnesium Alloy

Qiao Ke[1,2], Wang Kuaishe[1,2], Wang Wen[1,2], Li Tianqi[1,2], Wang Qiang[1,2], Yu Hailiang[3]

[1] *Xi'an University of Architecture and Technology, Xi'an 710055, China;* [2] *National and Local Joint Engineering Research Center for Functional Materials Processing, Xi'an 710055, China;* [3] *Center South University, Changsha 410083, China*

Abstract: Friction stir welding (FSW) has been validated to be a severe plastic deformation method for development of ultrafine-grained metals. In this study, hot-rolled AZ31 magnesium alloy plate was processed by FSW, and the effect of FSW on the low-cycle fatigue (LCF) behavior of AZ31 magnesium alloy was analyzed. The results show that the interface between the stir zone and thermo-mechanically affected zone at the advancing side is the weakest region, in which the monotonic tension and fatigue fracture occur. Compared with those of the base metal (BM), the LCF fatigue life, the yield strength, the ultimate tensile strength and the elongation of FSW specimen decrease. The main deformation during LCF is dislocation slip deformation. The fracture surface exhibits a typical fatigue characteristic with the fatigue striations. Finally, we found that the LCF behavior of BM and FSW specimens can be well described by the Coffin-Manson and Basquin's relations.

Key words: friction stir welding; magnesium alloy; texture; low-cycle fatigue; fracture

Magnesium (Mg) alloys, as light commercial structure material, have been widely used in automotive and rail transportation industries as a replacement of aluminum alloys and steels due to their low density, high specific strength, stiffness and good machinability[1-9]. However, it is difficult to obtain defect-free joints by the conventional fusion welding techniques, because the joint often exhibits many defects such as porosity, cracks, inclusions and oxidization.

As a solid-state welding technique, friction stir welding (FSW) has been successfully used for aluminum alloys[10,11], Mg alloys[12,13], copper alloys[14] and steels[15]. Compared with the traditional conventional fusion techniques, FSW can obtain a fine recrystallized microstructure with a higher ratio of high-angle grain boundaries and lower dislocation densities[16].

During industrial applications, Mg alloy components are usually used under cyclic loading or vibration. Therefore, it is crucial to investigate fatigue properties of Mg alloys[4,17]. Several studies about the fatigue behavior of FSW Mg alloys including stress-controlled high-cycle fatigue (HCF)[18,19] and strain-controlled low-cycle fatigue (LCF)[4,20-22] were reported in literatures. Chowdhury et al[18] studied the effect of pin thread orientation on the HCF strength of FSW joint of AZ31 Mg alloy. Naik et al[19] reported that the LCF fatigue life of FSW joint of AZ31 Mg alloy was affected by the welding parameters, and fatigue fracture occurred at the interface between the stir zone (SZ) and thermo-mechanically affected zone (TMAZ). Yang et al[20] also investigated the LCF behavior of FSW AZ31 Mg alloy, and the results show that the texture of joint has effect on the fatigue resistance and the fatigue fracture.

However, most researches focused on the HCF of FSW Mg alloys, and the LCF behavior of FSW Mg alloys is reported

Received date: March 13, 2018
Foundation item: National Natural Science Foundation of China (U1760201, 51574192, 51404180); The Xi'an Science and Technology Project (201805033YD11CG17(8))
Corresponding author: Wang Kuaishe, Ph. D., Professor, School of Metallurgical Engineering, Xi'an University of Architecture and Technology, Xi'an 710055, P. R. China, Tel: 0086-29-82205096, E-mail: wangkuaishe888@126.com

seldomly so far. Therefore, the aim of this study is to investigate the effect of FSW on the LCF behavior of AZ31 Mg alloy.

1 Experiment

The base metal used in this study is hot-rolled AZ31 (2.8Al-1.0Zn-0.2Mn, wt%) Mg alloy plates. The plates with a size of 200 mm×150 mm×4 mm were processed by FSW at a tool rotation rate of 1500 r/min and a travel speed of 47.5 mm/min. The cylindrical stir tool was made of W18Cr4V steel with a flat shoulder of 14 mm in diameter, a pin of 4 mm in diameter, and 3.8 mm in length. FSW experiments were performed on a vertical milling machine.

Microstructures of specimens, cross sections perpendicular to the FSW direction, were examined by optical microscope (OM, Olympus GX51) and electron backscattered diffraction (EBSD, Zeiss Merlin Compact). The specimens were ground, polished, and then etched using a solution of 5 g picric acid, 5 mL acetic acid, 10 mL H_2O and 90 mL ethanol. The macroscopic and microscopic textures were examined by X-ray diffraction (XRD, Bruker D8 Advance) and EBSD, respectively. The sample size for macroscopic texture examination is 5 mm×5 mm, and test size for microscopic texture test were 150 μm×130 μm and 700 μm×520 μm for FSW and BM specimens, respectively.

Dog-bone-shaped specimens for monotonic tensile and LCF testing were perpendicularly machined along the FSW direction with a parallel section of 25 mm×6 mm×3.5 mm (Fig.1). The monotonic tensile testing was conducted by an Instron-8801 test system with an initial strain rate of 10^{-3} s^{-1} at room temperature according to ASTM E8 standard[23]. LCF testing was also carried out in the Instron-8801 fatigue test system with a triangular waveform (R_ε=0) loading at a frequency of 0.5 Hz. The total strain amplitudes are 0.2%, 0.3%, 0.4%, 0.5% and 0.6%. After LCF test, the fracture surfaces of LCF specimens were observed by a scanning electron microscopy (SEM, JSM-6390A).

2 Results and Discussion

2.1 Microstructure

Cross-sectional macrostructure of FSW specimen is shown in Fig.2. Based on microstructure characteristics, FSW region can be divided into three zones: base metal (BM), stir zone (SZ), and thermo-mechanically affected zone (TMAZ). There is no obvious heat affected zone (HAZ) due to lower heat input and high cooling rate, which were result from the using of small-sized stir tool and thin AZ31 alloy plates.

The microstructure and {0002} pole figures of FSW specimen detected by EBSD in the different regions are shown in Fig.3. The BM (labeled region 3 in Fig.2) consists of coarse and non-uniform grains with several fine recrystallized grains distributed along the grain boundaries. The average grain size is about 30 μm. In addition, $\{10\bar{1}2\}\langle 10\bar{1}1\rangle$

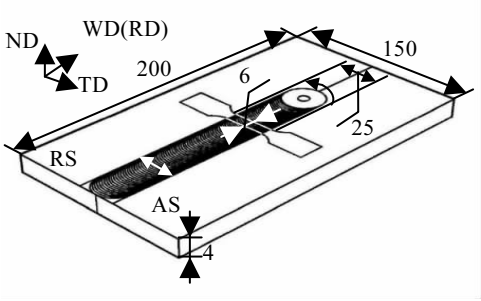

Fig.1 Illustration of FSW AZ31 plates showing tensile test and fatigue machining (ND presents normal direction; WD presents welding direction; RD presents rolling direction of BM; TD presents transversal direction. AS presents advancing side; RS presents retreating side. The AS of FSW specimen is where the rotation rate of the tool has the same direction as its travel speed whereas, on the RS, the two speed components have opposite directions) unit: mm

Fig.2 Cross-sectional macrostructure of FSW specimen

extension twins in the interior of coarse grains are confirmed by the misorientation angle distribution $\langle 10\bar{2}1\rangle$ 86° (misorientation with the Mg matrix). The SZ (labeled region 1 in Fig.2) is characterized by the fine and equiaxed recrystallized grains. The elongated grains are generated at the boundary between the SZ and TMAZ at the advancing side (SZ/TMAZ-AS) owing to shear deformation[24]. The average grain size in the SZ and SZ/TMAZ-AS regions is about 7 and 10 μm, respectively.

Fig.3 and Fig.4 show the microscopic and macroscopic textures of the BM and FSW specimens in the different regions, respectively. The *c*-axis of the BM is nearly parallel to TD direction, as shown in Fig.3d. It should be noted that the macroscopic texture of the BM detected by XRD (Fig.4a) shows evident rolling texture component, while it is not present in the pole figure measured by EBSD (Fig.3d). This mainly results from the limited grain numbers detected by EBSD in the limited analysis area. In addition, the SZ exhibits a significantly preferred grain orientation with the *c*-axis tilting to ND direction with an included angle of 30°~45° (Fig.3e). However, the grain orientation in the SZ/TMAZ-AS region changes with *c*-axis tilting to TD direction with an included angle of 35°~50° (Fig.3f). This

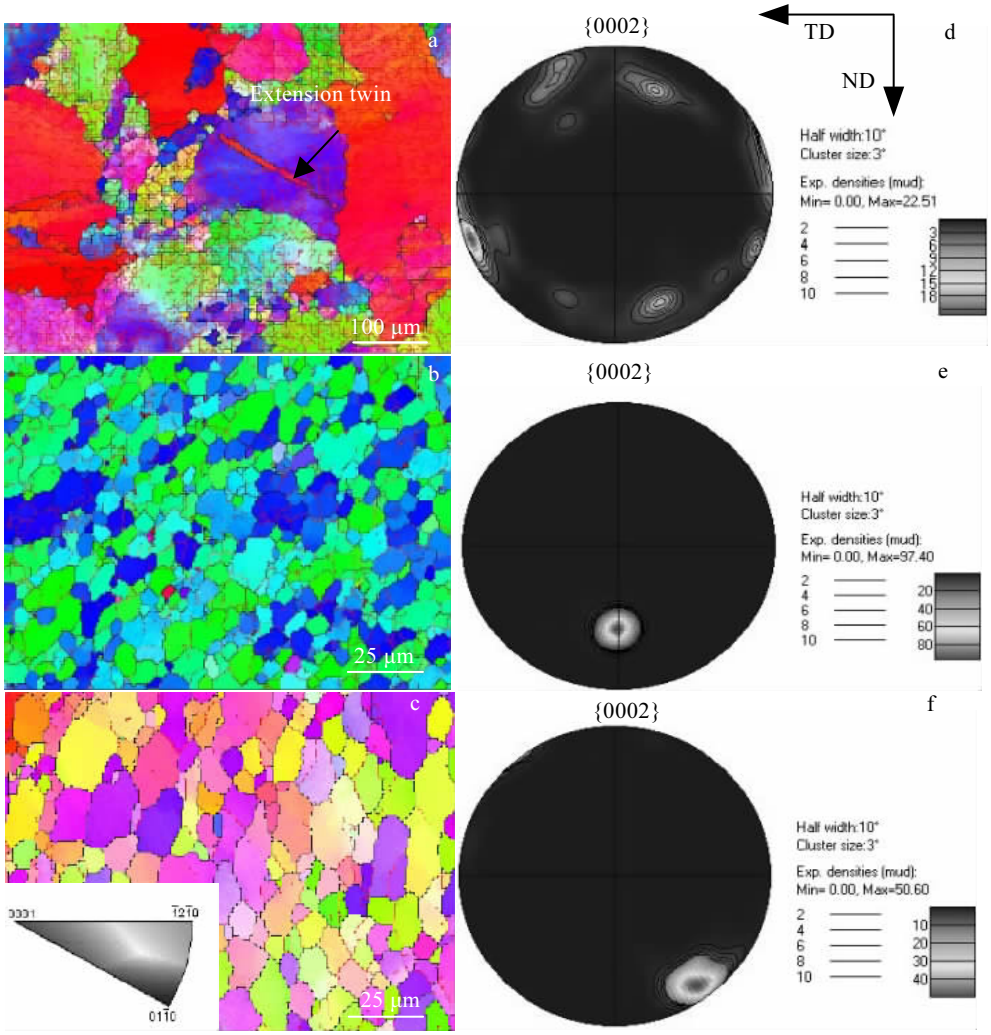

Fig.3 Microstructure (a~c) and {0002} pole figures (d~f) of FSW specimen detected by EBSD in different regions: (a, d) BM, (b, e) SZ, and (c, f) SZ/TMAZ-AS regions

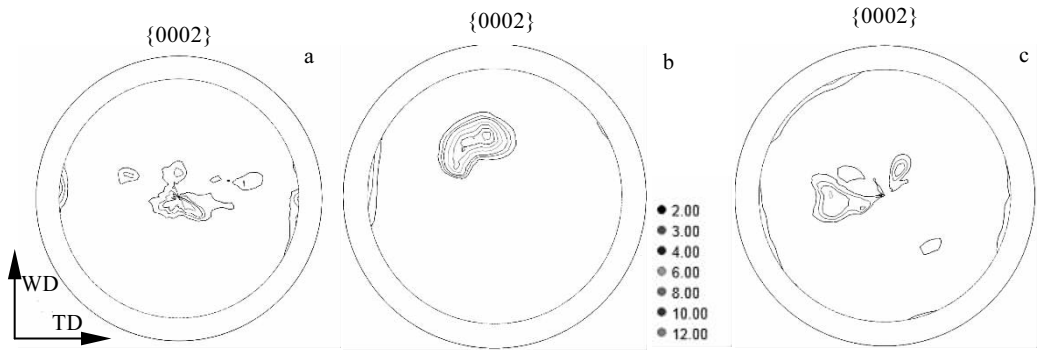

Fig.4 Incomplete {0002} pole figures of BM (a), SZ (b), and Z/TMAZ-AS regions detected by XRD (c)

result is mainly attributed to the different plastic deformation in the different regions. Furthermore, the macroscopic texture of the SZ (Fig.4b) and SZ/TMAZ-AS regions (Fig.4c) exhibits the similar grain orientation characteristics to the microscopic texture (Fig.3e and Fig.3f). It should be noted that the monotonic tension and LCF fracture occur in

the SZ/TMAZ-AS region. Thus, in this study, a detailed microstructure analysis has been conducted in this region while not in the interface between the SZ and TMAZ at the RS (SZ/TMAZ-RS).

During FSW, the material experiences severe plastic deformation and thermal exposure, which results in the formation of fine recrystallized grains, and an obvious basal texture in the processed region. In the SZ region, the rotation of *c*-axis is generated due to shear stress induced by the rotating pin and shoulder[25-27]. Woo et al[28] indicated that the rotating pin had a significant effect on the texture evolution, and produced a 90° rotation of the basal plane in the SZ region compared with the initial rolling texture in the BM region. The similar texture evolution was also reported in the FSW joint of AZ61 Mg alloy[29]. However, in this study, the *c*-axis tilted 30°~45° with respect to ND direction. This result is mainly attributed to the shear deformation near the upper surface induced only by the tool shoulder[17]. In a previous study, Yuan et al[25] indicated that the shear action of the shoulder diminished with the increase of the depth, and rotating pin started to dominate the texture through shear deformation. In addition, it should be noted that the *c*-axis tilted 35°~50° with respect to TD direction in the SZ/TMAZ-AS region, which results from the compressive stress induced by the shoulder. Similarly, in the literature[30], the *c*-axis titled almost 45°to TD direction for FSW joint.

2.2 Tensile properties

Fig.5 presents the microhardness distribution on the cross-section at the mid-thickness of FSW joint. The average microhardness (HV) of the BM is about 721 MPa. It is noted that the average microhardness in the SZ region is about 625 MPa, while the lowest microhardness about 565 MPa in the SZ/TMAZ-AS region.

The tensile properties of the BM and FSW specimens are listed in Table 1. The yield strength (YS), ultimate tensile strength (UTS) and elongation (EI.) of FSW specimen are lower than those of BM, and the tensile fracture occurs at the SZ/TMAZ-AS region. According to the strengthening theory of grain refinement, the fracture should be located in

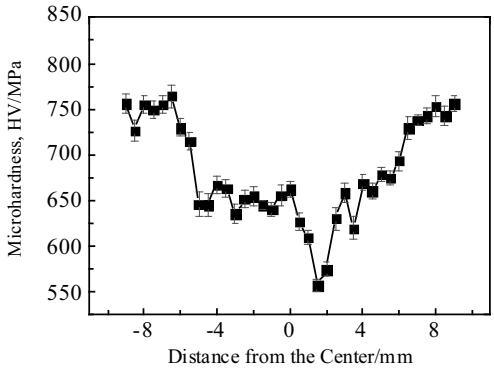

Fig.5 Microhardness distribution of the FSW joint

Table 1 Tensile properties of the BM and FSW joint

Specimen	YS/MPa	UTS/MPa	EI./%	Fracture location
BM	146.0±2.8	233.0±11.3	12.4±3.2	Middle section
FSW	95.0±2.8	196.5±6.3	10.3±0.2	SZ/TMAZ-AS region

the BM region because of its coarse microstructure. However, the fracture actually occurs at the SZ/TMAZ-AS region, because the texture predominates in the fracture [20, 28] (Fig.3 and Fig.4). At room temperature, basal slip normally has much lower critical resolved shear stress than prismatic and pyramidal slips, and thus it becomes the main deformation mechanism of Mg alloys. In addition, the Schmid factor (SF) had a significant effect on the activation of basal slip[20]. The SF distribution of basal slip for both BM and FSW specimens is shown in Fig.6. The average SF values in the BM, SZ and SZ/TMAZ-AS regions are 0.294, 0.048, and 0.425, respectively, which are consistent with the grain orientation distribution (Fig.3 and Fig.4). Therefore, the grain orientations in the SZ/TMAZ-AS region can be favor for basal slip, which is defined as a "soft grain orientation", and results in the fracture in this region. It can be concluded that the soft grain orientation in the SZ/TMAZ-AS region reduces the tensile properties of FSW joint.

2.3 Cyclic stress-strain response

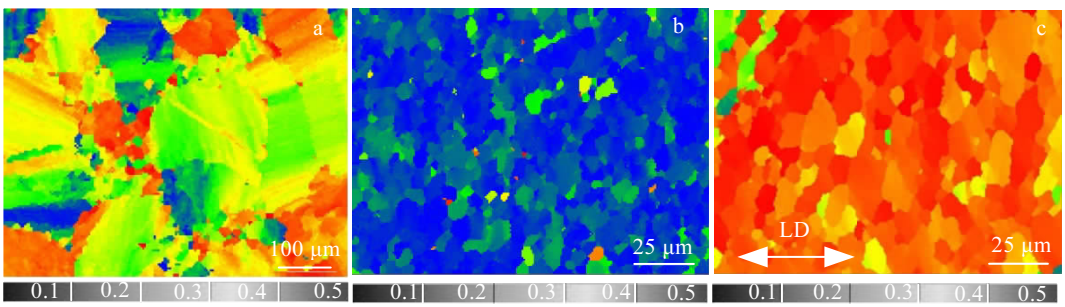

Fig.6 Schmid factor distribution of basal slip for BM (a), SZ (b), and SZ/TMAZ-AS regions (c) (LD presents fatigue loading direction)

Fig.7 shows the stress amplitudes of both BM and FSW specimens with respect to the number of cycles at various total strain amplitudes. It can be clearly seen that stress amplitudes of both the BM and FSW specimens increase with the increase of the total strain amplitude. Moreover, FSW specimens exhibit a lower stress amplitude compared to the BM with the same total amplitude and the number of cycles. It should be noted that the BM exhibits a nearly constant stress amplitude with respect to the number of cycles at the total strain amplitudes of 0.2%, indicating that the BM mainly produces the elastic deformation at the lower total strain amplitude. In contrast, the FSW specimens exhibit cyclic hardening at the same total strain amplitude (0.2%). This result is consistent with the cyclic stress-strain response of fine-grained AZ31 alloy produced by other SPD techniques[1, 9, 31-33].

Fig.8 shows the typical hysteresis loops of the first, second and mid-life cycles at the total strain amplitude of 0.5% of both BM and FSW specimens. It can be clearly seen that the shape of hysteresis loops during LCF deformation is nearly symmetric for both the BM and FSW specimens, indicating that dislocation slip is the main LCF deformation mechanism in this study.

Fig.9 shows the OM microstructure of BM and FSW specimens after fatigue failure in the area near the fracture surface. It can be clearly observed that both the BM and FSW specimens exhibit several twins, indicating that the twinning is one of deformation mechanisms during LCF deformation. Moreover, the shape of hysteresis loops of both BM and FSW specimens (Fig.8) is nearly symmetric with no obvious distortion. This suggests that dislocation slip predominates in LCF deformation[34, 35].

Both grain size and grain orientation have the significant effect on the twinning deformation. On the one hand, twinning is prone to take place in the coarse grains[36]. On the other hand, twining is sensitive to the grain orientation. For example, $\{10\bar{1}2\}<10\bar{1}1>$ tensile twinning is easily acti-

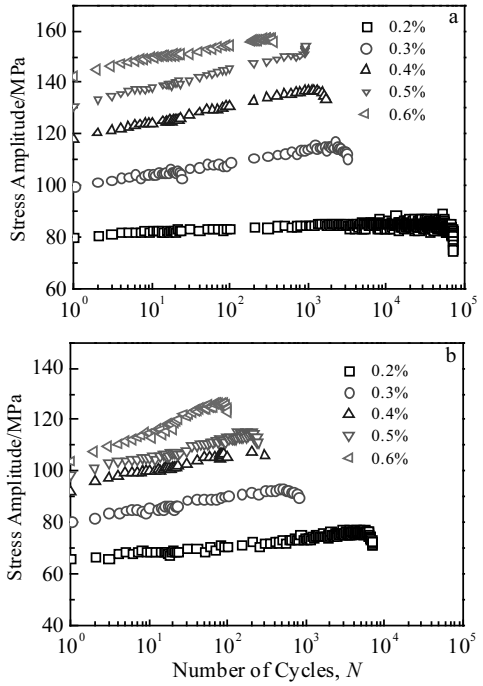

Fig.7 Stress amplitude vs number of cycles of specimens at various total strain amplitudes: (a) BM and (b) FSW

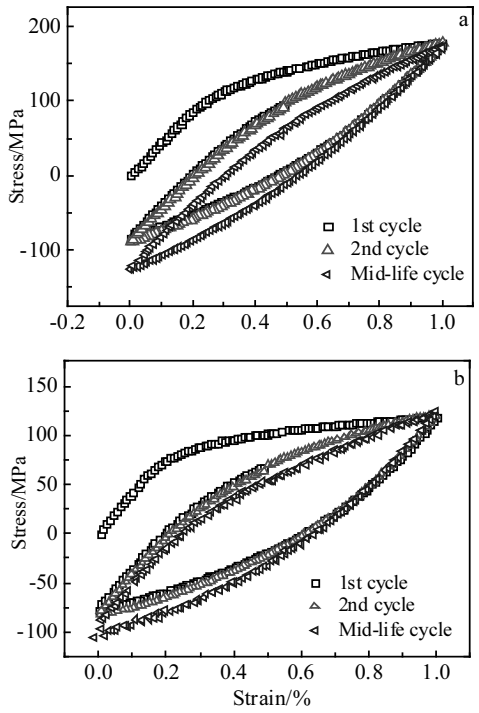

Fig.8 Typical hysteresis loops of BM (a) and FSW (b) specimens at the total strain amplitude of 0.5%

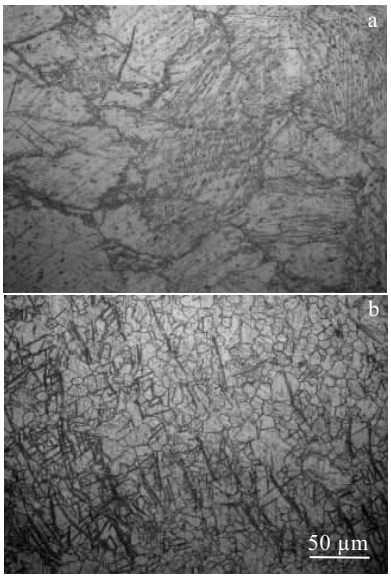

Fig.9 OM images of BM (a) and FSW (b) specimens after fatigue failure in the area near the fracture surface

vated when tensile direction is parallel to the *c*-axis, or compressive direction is perpendicular to the *c*-axis[37, 38-41].

In a previous study, Yang et al[27] studied the LCF behavior of FSW AZ31 alloy. They reported that the average grain size of SZ region was refined to approximately 20 μm, exhibiting a slight twining-detwinning phenomenon during LCF deformation. By contrast, there was an obvious twining-detwinning phenomenon in the interior of coarse grains with the average size of 150 and 56 μm [9, 18]. In this study, FSW results in the grain refinement with the average grain size of 7 and 10 μm in the SZ (Fig.3b) and SZ/TMAZ-AS regions, respectively (Fig.3c). Accordingly, it can be inferred that grain refinement is responsible for the slight twinning of FSW specimen during LCF deformation. As for the BM specimen, on the one hand, initial rolling texture is not prone to activate twinning deformation. On the other hand, the fine grains are distributed along the grain boundaries which impedes the twinning deformation (Fig.9).

2.4 Fatigue life and parameters

Fig.10 shows the total strain amplitudes of both BM and FSW specimens as a function of the numbers of cycles to failure. The fatigue life of both the BM and FSW specimens decreases with the increase of the total strain amplitude. Meanwhile, FSW specimens have much shorter fatigue life than the BM specimen at the given total strain amplitude.

The cyclic stress-strain curve can be described by the following equation[4, 20, 37]:

$$\frac{\Delta\sigma}{2} = K'(\frac{\Delta\varepsilon_p}{2})^{n'} \quad (1)$$

Where K' is the cyclic strength coefficient, n' is the cyclic strain hardening exponent, $\Delta\sigma/2$, and $\Delta\varepsilon_p/2$ are the stress amplitude and plastic strain amplitude at the mid-life cycle, respectively.

Fig.11a shows the stress amplitude vs plastic strain amplitude for both BM and FSW specimens at the mid-life cycle. Fig.11b and Fig.11c show the elastic and plastic strain amplitudes at the mid-life cycle vs the number of cycles to failure for both BM and FSW specimens. According to the Basquin and Coffin-Manson relations[1-4, 20], the relationships between the total strain amplitude $\Delta\varepsilon_t/2$, plastic strain amplitude $\Delta\varepsilon_p/2$, and elastic amplitude $\Delta\varepsilon_e/2$, can be expressed by the following equation:

$$\frac{\Delta\varepsilon_t}{2} = \frac{\Delta\varepsilon_e}{2} + \frac{\Delta\varepsilon_p}{2} \quad (2)$$

The first item on the right-hand side of the equation can be expressed by the Basquin equation:

$$\frac{\Delta\varepsilon_e}{2} = \frac{\sigma_f'(2N_f)^b}{E} \quad (3)$$

and the second item can be expressed by the Coffin-Manson equation:

$$\frac{\Delta\varepsilon_p}{2} = \varepsilon_f'(2N_f)^c \quad (4)$$

Then,

$$\frac{\Delta\varepsilon_t}{2} = \frac{\sigma_f'(2N_f)^b}{E} + \varepsilon_f'(2N_f)^c \quad (5)$$

Where E is the Young's modulus, N_f the number of cycles to failure, σ_f' the fatigue strength coefficient, b the fatigue strength exponent, ε_f' the fatigue ductility coefficient, and c the fatigue ductility exponent.

The fatigue life parameters calculated by the Eqs.(1) and (5) are summarized in Table 2. It can be seen that the cyclic

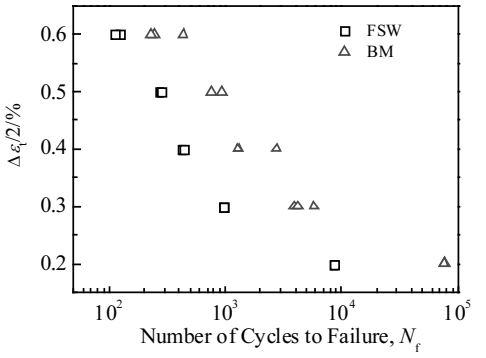

Fig.10 Total strain amplitudes of the BM and FSW specimens as a function of the numbers of cycles to failure

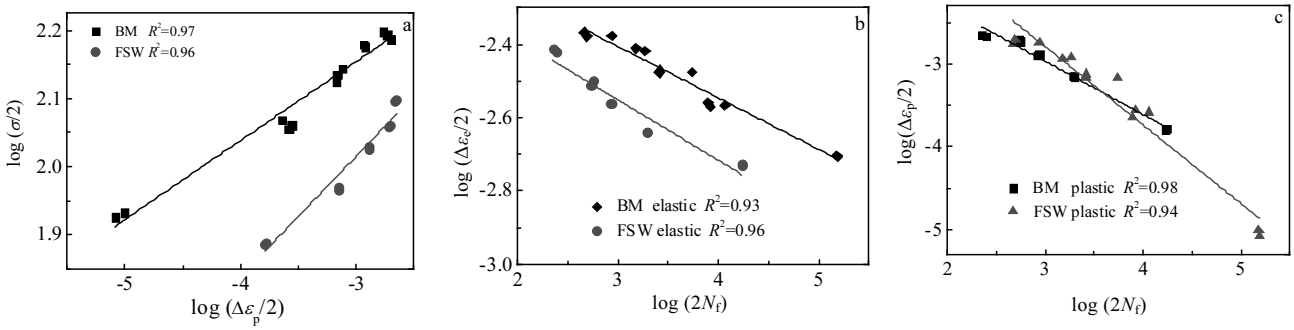

Fig.11 Evaluation of the fatigue parameters for both the BM and FSW specimens: (a) stress amplitude (σ/2) vs plastic strain amplitude ($\Delta\varepsilon_p$/2) at the mid-life cycle; (b) elastic strain amplitudes ($\Delta\varepsilon_e$/2) vs the number of cycles ($2N_f$) to failure at the mid-life cycle; (c) plastic strain amplitudes ($\Delta\varepsilon_p$/2) vs the number of cycles ($2N_f$) to failure at the mid-life cycle

Table 2 LCF parameters of both BM and FSW specimens

Low cycle fatigue parameters	FSW	BM
Cyclic strain hardening exponent, n'	0.17	0.12
Cyclic strength coefficient, K'/MPa	350	318
Fatigue strength coefficient, σ_f'/MPa	394	467
Fatigue strength exponent, b	-0.16	-0.14
Fatigue ductility coefficient, ε_f'	0.09	1.14
Fatigue ductility exponent, c	-0.64	-0.95

Fig.12 Cross-sectional macrostructure of FSW specimen after fatigue test

strain hardening exponent n' of the FSW specimens is higher than that of the BM. This reveals that the FSW specimens have more evident cyclic hardening than the BM specimens, which is consistent with the results plotted in Fig.6. The absolute value of fatigue ductility exponent c of the BM is higher than that of FSW specimen, indicating that BM has higher LCF performance (Fig.9).

2.5 Fractography

Fig.12 shows the cross-sectional macrostructure of FSW specimen after fatigue test. The fatigue fracture of FSW specimens occurs in the SZ/TMAZ-AS region, and there is an obvious necking phenomenon in the SZ/TMAZ-AS region. In a previous study, Naik[19] and Yang et al[20] reported that the fatigue cracks of FSW AZ31 alloy propagated from the TMAZ to SZ region, and finally fractured in the SZ region. However, in this study, the fatigue cracks mainly propagated through the SZ/TMAZ-AS region owing to the soft grain orientation.

Fig.13 shows the fracture surface of both BM and FSW specimens at the total strain amplitude of 0.4%, including the crack initiation, propagation and final fracture regions. The fatigue cracks of both the BM and FSW specimens initiated at the specimen surface. Fig.13a shows the fracture surface of the BM in the crack initiation region. It can be clearly seen that there is a rough surface with heterogeneous facets, which was related to the non-uniform microstructure (Fig.3a). The fracture surface of FSW specimen consists of some facets (Fig.13b). For both the BM and FSW specimens, the crack propagation zones are mainly characterized by the fatigue striations (Fig.12c and Fig.12d). In the final fracture region, both the BM and FSW specimens exhibit a dimple fracture surface typical of ductile failure (Fig.13e and Fig.13f).

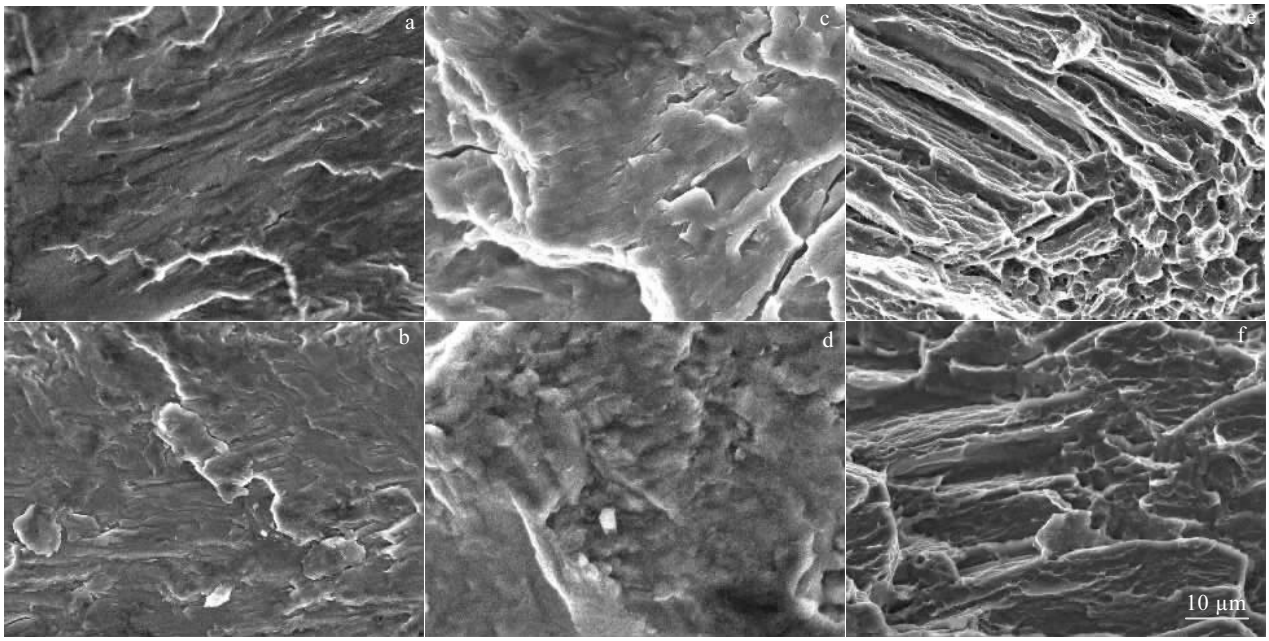

Fig.13 Fatigue fracture surfaces of crack initiation region(a, b), crack propagation region(c, d), and final fracture region (e, f) at the total strain amplitude of 0.4% of the BM (a, c, e) and FSW specimens (b, d, f)

3 Conclusions

1) The SZ/TMAZ-AS region is the weakest region where the monotonic tension and fatigue fracture occur. Compared with the BM, the yield strength, ultimate tensile strength and elongation of the FSW specimen decrease, which are mainly attributed to the soft grain orientation.

2) Compared with the BM specimens, LCF fatigue life of FSW specimens decreases at the same total strain amplitude. The main deformation during LCF deformation is dislocation slip. LCF behavior of BM and FSW specimens can be well described by the Coffin-Manson and Basquin's relations.

3) The fatigue fracture of FSW specimens mainly occurs at the SZ/TMAZ-AS region owing to the soft grain orientation. The fracture surface exhibits a typical fatigue characteristic with the fatigue striations.

References

1 Hasegawa S, Tsuchid Y, Yano H *et al. International Journal of Fatigue*[J], 2007, 29: 1839

2 Park S H, Hong S G, Lee B H *et al. International Journal of Fatigue*[J] 2010, 32: 1835

3 Tian D D, Liu X S, He G Q *et al. Materials Science and Engineering A*[J], 2016, A654: 60

4 Ni D R, Chen D L, Yang J *et al. Materials and Design*[J], 2014, 56: 1

5 Mirza F A, Chen D L, Li D J *et al. Materials and Design*[J], 2014, 64: 63

6 Chen G , Lu LT, Cui Y *et al. International Journal of Fatigue*[J], 2015, 80: 364

7 Zhu R, Cai X, Wu Y *et al. Materials and Design*[J], 2014, 53: 992

8 Lv F, Yang F, Duan Q Q *et al*. *Scripta Materialia*[J], 2009, 61: 887

9 Begum S, Chen D, Xu S *et al*. *International Journal of Fatigue*[J], 2009, 31: 726

10 Mao Y Q, Ke L M, Chen Y H *et al*. *Journal of Materials Science and Technology*[J], 2018, 34(1): 228

11 Guo N, Fu Y L, Wang Y Z *et al*. *Materials and Design*[J], 2017, 113: 273

12 Ugender S. *Journal of Magnesium and Alloys*[J], 2018, 6(2): 205

13 Mironov S, Onuma T, Sato Y S *et al. Materials Characterization*[J], 2017, 130: 1

14 Kush P M, Vishvesh J B. *Journal of Materials Processing Technology*[J], 2017, 239: 336

15 Venkatesh K M, Arivarsu M, Manikandan M A *et al*. *Materials Today: Proceedings*[J], 2018, 5(5) : 13227

16 Kumar N, Mishra R, Huskamp C S *et al. Materials Science and Engineering A*[J], 2011, 528: 5883

17 Mishra R S, Ma Z Y. *Materials Science and Engineering R*[J], 2005, 50: 1

18 Chowdhury S M, Chen D L, Bhole S D *et al*. *Proceedia Engineering*[J], 2010, 2(1): 825

19 Naik B S, Chen D L, Cao X M *et al. Metallurgical and Materials Transactions A*[J], 2013, 44: 3732

20 Yang J, Ni D R, Wang D *et al*. *Metallurgical and Materials Transactions A*[J], 2013, 45: 2101

21 Dallmeier J, Denk J, Huber O *et al*. *International Journal of Fatigue*[J], 2015, 80: 306

22 Geng C J, Wu B L, Du X H *et al*. *Transactions of Nonferrous Metals Society of China*[J], 2013, 23: 1589

23 *Standard Test Methods for Tension Testing of Metallic Materials, ASTM Standards T68*[S]. 2015

24 Hu Z L, Wang X S, Yuan S J. *Materials Characterization*[J], 2012, 73: 114

25 Yuan W, Mishra R S, Carlson B *et al*. *Scripta Materialia*[J], 2011, 64: 580

26 Mironov S, Onuma T, Sato Y S *et al. Acta Materia*[J], 2015, 100: 301

27 Xin R L, Zheng X, Liu Z *et al. Journal of Alloys and Compounds*[J], 2016, 659: 51

28 Woo W, Choo H, Brown D W *et al*. *Scripta Materialia*[J], 2006, 54: 1859

29 Park S H C, Sato Y S, Kokawa H. *Metallurgical and Materials Transactions A*[J], 2003, 34A: 987

30 Xin R L, Liu D J, Shu X G *et al. Journal of Alloys and Compounds*[J], 2016, 670: 64

31 Kwon S, Song K, Shin K S *et al. Transactions of Nonferrous Metals Society of China*[J], 2010, 20: 533

32 Chen C, Liu T, Lv C *et al*. *Materials Science and Engineering A*[J], 2012, 539: 223

33 Zhu R, Wu Y J, Ji W Q *et al*. *Materials Letters*[J], 2011, 65: 3593

34 Yin S M, Yang H J, Li S X *et al*. *Scripta Materialia*[J], 2008, 58: 751

35 Koike J, Fujiyama N, Ando D *et al*. *Scripta Materialia*[J], 2010, 63: 747

36 Huang G S, Li J H, Han T Z *et al*. *Materials and Design*[J], 2014, 58: 439

37 Mokdad F, Chen D L. *Materials and Design*[J], 2015, 67: 436
38 Hong S G, Park S H, Lee C S. *Journal of Materials Research*[J], 2010, 25: 784
39 Barnett M R, Bouaziz O, Toth L S. *International Journal of Plasticity*[J], 2015, 72: 151
40 Wu W, An K. *Journal of Alloys and Compounds*[J], 2016, 656: 539
41 Wu L, Jain A, Brown D W *et al*. *Acta Materia*[J], 2008, 56: 688

搅拌摩擦焊接 AZ31 镁合金低周疲劳性能

乔　柯[1,2]，王快社[1,2]，王　文[1,2]，李天麒[1,2]，王　强[1,2]，喻海良[3]
(1. 西安建筑科技大学，陕西　西安　710055)
(2. 功能材料国家地方联合工程研究中心，陕西　西安 710055)
(3. 中南大学，湖南　长沙　410083)

摘　要：作为新型大塑性变形技术，搅拌摩擦焊接技术（FSW）已成功应用于超细晶材料的制备。采用 FSW 对热轧态 AZ31 镁合金进行连接，对母材和 FSW 接头的低周疲劳性能进行了研究。结果表明：在疲劳和单轴拉伸测试过程中，焊合区与前进侧热机械影响区交界处为性能薄弱区域。FSW AZ31 接头的低周疲劳寿命、屈服强度、抗拉强度以及断后延伸率均低于母材。AZ31 镁合金疲劳测试过程中的主要变形机制为位错滑移，疲劳断口表面呈现出明显的疲劳纹。最终，发现母材和 FSW 接头低周疲劳行为符合 Coffin-Manson 和 Basquin 关系。

关键词：搅拌摩擦焊接；镁合金；织构；低周疲劳；断口

作者简介：乔　柯，男，1990 年生，硕士，助教，西安建筑科技大学冶金工程学院，陕西　西安　710055，电话 029-82202923，E-mail: qiaokemarshal@126.com